The effects of chromium substitution on the electronic and magnetic properties of $CuFeO_2$

PINAR EZIRCAN[1], M. SELIM ASLAN[2], MUSTAFA AKYOL[3], HIDETOSHI MIYAZAKI[4], O. MURAT OZKENDIR[5,*], AHMET EKICIBIL[2], HAKAN OZTURK[1]

[1]*Faculty of Engineering and Natural Sciences, Department of Physics, Osmaniye Korkut Ata University, 80000, Osmaniye, Turkey*

[2]*Department of Physics, Faculty of Science and Letters, Çukurova University, Adana, Turkey*

[3]*Department of Materials Science and Engineering, Faculty of Engineering, Adana Alparslan Turkes Science and Technology University, Adana, Turkey*

[4]*Department of Physical Science and Engineering, Nagoya Institute of Technology, 466-8555 Nagoya, Japan*

[5]*Department of Mathematical and Natural Sciences, Tarsus University, 33400, Tarsus, Turkey*

We present a comprehensive investigation of chromium-substituted delafossite $CuFe_{1-x}Cr_xO_2$ using synchrotron X-ray diffraction (SR-XRD), X-ray absorption fine structure (XAFS) spectroscopy, and physical property measurements (10-300 K). The studied pristine $CuFeO_2$ exhibits a stable dual-phase structure comprising dominant trigonal-rhombohedral (R-3m, 87.7 wt%) and minor hexagonal ($P6_3/mmc$, 12.3 wt%) polymorphs, which persists throughout chromium substitution. Structural analysis reveals chromium incorporation nucleates a secondary hexagonal $CuCrO_2$ phase ($P6_3/mmc$) while preserving the host matrix's oxygen stoichiometry, attributable to stronger Fe-O versus Cr-O bonding. XAFS confirms maintained Fe^{3+} coordination geometry and minimal framework disruption despite Cr substitution. Remarkably, all substituted samples display soft ferromagnetism throughout 10-300 K, contrasting with pure $CuFeO_2$'s antiferromagnetic ordering below 11-14 K. This emergent ferromagnetism originates from competing exchange interactions, where introduced ferromagnetic Cr^{3+}-O-Cr^{3+} pathways (J ≈ +15.4 K) coexist with native antiferromagnetic Fe^{3+}-O-Fe^{3+} couplings (J ≈-8.2 K). The findings demonstrate chromium's dual role as both structural stabilizer and magnetic modifier in delafossite oxides.

(Received October 7, 2024; accepted June 4, 2025)

Keywords: Oxides, Magnetic materials, XAFS, PPMS

1. Introduction

Driven by breakthroughs in quantum materials and spintronics, intensive research is focused on designing materials with tunable electronic and magnetic properties for next-generation technologies, including low-power computing, spin-based memory devices, and energy-efficient sensors [1–3]. A critical challenge in this field is achieving precise control over magnetic behavior under varying external conditions, particularly for spintronic applications where spin-polarized transport and magnetic switching are essential [4, 5]. Among the most promising candidates is $CuFeO_2$, a delafossite oxide that exhibits intriguing antiferromagnetic (AFM) ordering below 11 K [2], as well as multiferroic behavior under applied magnetic fields [6].

Cu-based delafossites (general formula ABO_2, where A = Cu^+ and B = Fe^{3+}, Cr^{3+}, or Al^{3+}) have attracted considerable interest due to their multifunctional properties, including thermoelectricity (high Seebeck coefficient and low thermal conductivity) [5, 6], p-type transparent conductivity (for optoelectronic applications) [7-9], gas sensing and catalytic activity (due to surface redox-active Fe^{3+} sites) [10], energy storage (as electrode materials for batteries and supercapacitors) [11].

While $CuFeO_2$ remains the most studied delafossite, recent studies have revealed novel phenomena, such as electric-field-controlled magnetism and spin-lattice coupling, which are critical for voltage-tunable spintronic devices [12-14]. Its hexagonal layered structure (Fig. 1a, b) consists of alternating FeO_6 octahedral layers and Cu^+-O dumbbells, creating a natural spin-frustrated geometry that enables exotic magnetic phases, including partially disordered antiferromagnetic (PDAF) states and spin-flop transitions under high fields [15].

The electronic and magnetic properties of $CuFeO_2$ are highly sensitive to oxygen stoichiometry and cation off-stoichiometry, which can induce charge carrier modulation and defect-mediated magnetism [2]. Recent advances in thin-film epitaxy and chemical doping (e.g., Mg^{2+} or Al^{3+} substitution) have further enhanced its conductivity and magnetic anisotropy, making it suitable for room-temperature spintronic applications [16].

Iron (Fe^{3+}), as a 3d transition metal, plays a decisive role in defining the spin and electronic structure of delafossites. Its high-spin state (S = 5/2) contributes to strong superexchange interactions, while spin-orbit coupling enables Dzyaloshinskii-Moriya interactions (DMI), which are crucial for stabilizing non-collinear spin textures and topological magnetic defects [17]. Recent neutron scattering and first-principles calculations have

uncovered unconventional magnon excitations in $CuFeO_2$, suggesting potential for magnon-driven spin transport in quantum devices [16].

All the aspects of use in technological needs evolve the understanding importance of $CuFeO_2$ as a versatile platform for exploring quantum magnetism, multiferroicity, and spin-caloritronic effects, with significant implications for future energy-efficient and quantum technologies [15-17].

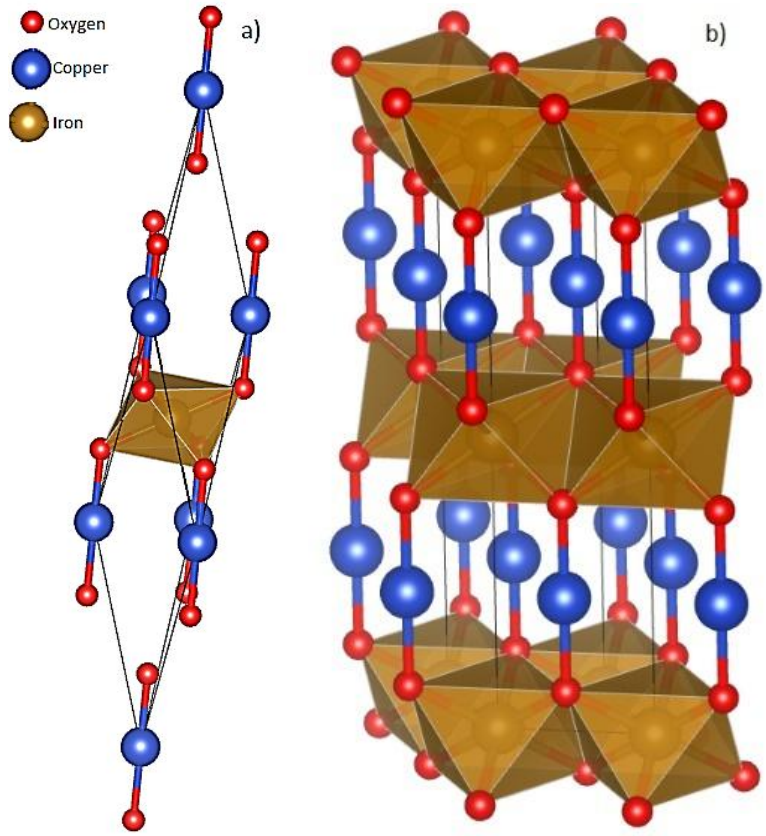

Fig. 1. Crystal structure representations of delafossite $CuFeO_2$ showing: (a) The trigonal-rhombohedral phase (space group $R\bar{3}m$) with alternating layers of edge-sharing FeO_6 octahedra and linearly coordinated Cu^+ ions; (b) The hexagonal polymorph (space group $P6_3/mmc$) featuring a distinct stacking sequence of FeO_6 layers (colour online)

This study focuses on $CuFeO_2$, an antiferromagnetic (AFM) semiconductor with a hexagonal delafossite structure (space group $R\bar{3}m$), which has garnered attention due to its geometric frustration, spin-phonon coupling, and tunable electronic structure under chemical substitution. To systematically explore the effects of spin and charge modulation, we synthesized a series of Cr^{3+}-substituted $CuFe_{1-x}Cr_xO_2$ (x = 0.0, 0.01, 0.02, 0.05, 0.10, 0.20) powders via a sol-gel method, ensuring homogeneous cation distribution and controlled stoichiometry, which is critical for minimizing secondary phases and defect-related artifacts.

The crystal structure and phase purity of the synthesized samples were rigorously analyzed using high-resolution synchrotron X-ray diffraction (SR-XRD) at the Fe K-edge, providing exceptional sensitivity to lattice distortions, site occupancies, and anisotropic thermal parameters. Synchrotron radiation was essential for resolving subtle structural modifications induced by Cr doping, particularly in detecting local symmetry breaking and cation off-centering, which influence magnetic exchange pathways. Moreover, SR-XRD technique enables Rietveld refinement with ultra-high resolution (<0.001 Å in d-spacing), critical for detecting subtle lattice strains induced by Cr^{3+} (0.615 Å) substitution for Fe^{3+} (0.645 Å) in octahedral sites.

Complementary X-ray absorption fine structure spectroscopy (XAFS) was employed to probe the electronic structure, oxidation states, and local coordination environment of Fe and Cr. XAFS is uniquely powerful for such investigations due to its element-specificity, short-range order sensitivity, and ability to distinguish between crystallographic and electronic contributions to spectral features. Our combined SR-XRD and XAFS approach provides unprecedented insight into how local structural distortions and electronic reorganization govern macroscopic properties in $CuFe_{1-x}Cr_xO_2$, advancing the design of tailored magnetic semiconductors.

By the analyzing the magnetic behaviors of $CuFeO_2$, supports the understanding of the background mechanism of modifying the spin frustration by introducing competing

AFM (Fe^{3+}–O–Fe^{3+}) and FM (Cr^{3+}–O–Cr^{3+}) interactions, leading to spin-glass behavior at low temperatures.

2. Materials and methods

A series of chromium-substituted delafossite oxides with the composition $CuFe_{1-x}Cr_xO_2$ (x= 0.00, 0.01, 0.05, 0.10, 0.15, and 0.20) were synthesized via a modified sol-gel method to ensure high phase purity and homogeneous cation distribution. High-purity precursor powders—Cu_2O (Sigma-Aldrich, >99.99%), α-Fe_2O_3 (hematite, >99.99%), and Cr_2O_3 (>99.99%) were stoichiometrically weighed and dispersed in anhydrous ethanol to minimize hydroxyl contamination. The suspension was magnetically stirred at 850 rpm for 12 hours to achieve a colloidally stable mixture, followed by dissolution in dilute HNO_3 (0.1 M) under continuous stirring for 2 hours at 298 K to promote precursor complexation.

The resulting sol was thermally treated at 80 °C for one hour to initiate polycondensation, forming a viscous gel that was subsequently dried at 110 °C for 24 hours to yield a porous xerogel. The dried product was manually ground using an agate mortar (to avoid Fe contamination) and subjected to a two step calcination process. In the first step, pre-annealing at 400 °C for 6 hours (heating rate: 5 °C/min) to decompose residual nitrates and organics performed. In the second step, final sintering at 850 °C for 24 hours in a static air atmosphere to ensure complete crystallization into the delafossite phase ($R\bar{3}m$ symmetry), with intermediate grinding to enhance reactant homogenization performed.

High-resolution powder X-ray diffraction (PXRD) data were collected at BL02B2 of the SPring-8 synchrotron facility (Hyogo, Japan), a beamline optimized for high-energy X-rays (12–37 keV) and charge density studies. The experimental setup include a Debye-Scherrer camera with a high-sensitivity image plate detector for wide-angle coverage. Six MYTHEN-II microstrip detectors for simultaneous high-count-rate data acquisition, ensuring excellent angular resolution ($\Delta 2\theta <$ 0.001°) and statistical precision. A capillary sample stage (0.3 mm diameter) spun at 1 Hz to minimize preferred orientation effects. The $\lambda = 0.5$ Å incident beam (calibrated using NIST Si 640c) enabled Rietveld refinement with sub-ångström sensitivity to lattice parameter shifts and secondary phase detection (e.g., CuO, Fe_3O_4). Data were processed using GSAS-II, with peak-shape modeling accounting for synchrotron-specific instrumental broadening [13].

XAFS measurements were performed at BL01B1 (SPring-8), a dedicated XAFS beamline with capabilities for transmission, fluorescence, and surface-sensitive detection modes. The energy range of the beamline is 3.8–113 keV, covering K-edges of Fe (7.112 keV) and Cr (5.989 keV) with a detector suite of Lytle detector (ionization chambers) for bulk-sensitive transmission XAFS. For the XAFS fluorescence yield mode data collection, a 19-element Ge solid-state detector used (minimizing self-absorption). Moreover, a PILATUS 100K detector can be used for depth-resolved grazing-incidence XAFS (probing ~5–50 nm surface layers) data collection. On the beamline, cryostats (10–300 K) and furnaces (up to 1000 °C) can be used for temperature-dependent studies [14].

The magnetic behavior of $CuFe_{1-x}Cr_xO_2$ was characterized using a Quantum Design PPMS-9T equipped with a Vibrating Sample Magnetometer (VSM). Experimental protocols included in the study were as follows:

i) Zero-field-cooled (ZFC) and field-cooled (FC) M(T) curves (10–300 K, H = 100 Oe) to identify AFM transitions (T_N) and spin-glass signatures.

ii) M(H) hysteresis loops (±3 kOe, 10 K) to assess coercivity (H_c) and saturation magnetization (M_s), with diamagnetic background subtraction.

iii) AC susceptibility (f = 10–1000 Hz) to probe spin dynamics near critical doping ($x \geq 0.10$).

3. Results and discussion

Synchrotron X-ray diffraction analysis confirmed the polycrystalline nature of all synthesized $CuFe_{1-x}Cr_xO_2$ samples. Rietveld refinement revealed that the undoped base material (x = 0.00) crystallized predominantly in the trigonal-rhombohedral delafossite structure (space group $R\bar{3}m$, 87.7 wt%), with a secondary hexagonal phase (space group $P6_3/mmc$, 12.3 wt%) present due to alternative stacking sequences along the c-axis (Table 1). This dual-phase configuration remained stable across the entire compositional series, indicating robust phase coexistence under the employed synthesis conditions.

The invariance of primary peak positions in the $R\bar{3}m$ phase following chromium substitution demonstrates that Cr^{3+} ions do not incorporate significantly into the Fe^{3+} sites of the $CuFeO_2$ lattice. Instead, chromium preferentially forms a distinct hexagonal $CuCrO_2$ phase ($P6_3/mmc$ symmetry), as evidenced by the systematic appearance of new diffraction peaks corresponding to this phase in all doped samples. This phase segregation behavior suggests limited solid solubility of Cr in the $CuFeO_2$ matrix, likely due to the substantial differences in ionic radii between Fe^{3+} (0.645 Å) and Cr^{3+} (0.615 Å) in octahedral coordination, as well as differences in their electronic configurations.

The XRD patterns of Cr-substituted samples (Fig. 2) exhibit three key features: (a) preservation of the original $CuFeO_2$ $R\bar{3}m$ phase fingerprint peaks, (b) emergence of characteristic $CuCrO_2$ $P6_3/mmc$ reflections with increasing Cr content, and (c) absence of peak shifting in the primary phase, confirming the formation of a phase-separated system rather than a true solid solution. The consistent phase fraction ratio between the $R\bar{3}m$ and $P6_3/mmc$ components (±2% variation across the series) further supports this interpretation, indicating that the Cr substitution primarily promotes the nucleation of discrete $CuCrO_2$ domains rather than modifying the existing $CuFeO_2$ crystal structure.

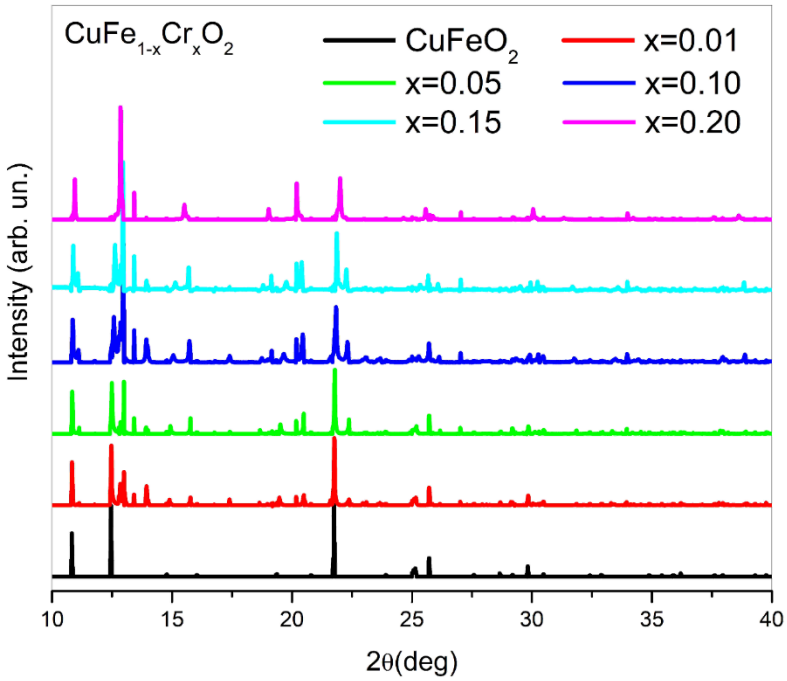

Fig. 2. Synchrotron X-ray diffraction patterns of the $CuFe_{1-x}Cr_xO_2$ series (x = 0.00-0.20) showing 2θ range (10-40°) demonstrating phase evolution with chromium substitution (colour online)

The lattice parameters of trigonal-rhombohedral $CuFeO_2$ exhibit contraction upon chromium incorporation, attributable to the smaller ionic radius of Cr^{3+} (0.615 Å) compared to Fe^{3+} (0.645 Å) in octahedral coordination. However, when chromium substitutes at non-iron lattice sites, a slight but measurable expansion of the unit cell occurs with increasing chromium content. This contrasting behavior suggests two distinct substitution mechanisms: isovalent replacement at Fe sites causing lattice contraction, and interstitial incorporation leading to structural expansion. In contrast, the hexagonal $CuFeO_2$ phase shows progressive lattice contraction, particularly for chromium concentrations ≤10%. This systematic variation indicates direct Cr^{3+} substitution at Fe^{3+} sites within the hexagonal structure, where chromium ions interact strongly with the surrounding oxygen coordination sphere. The differing response between phases highlights chromium's preferential site occupation, while it primarily substitutes for iron in the hexagonal structure, it appears to occupy both substitutional and interstitial sites in the trigonal-rhombohedral phase. Notably, at chromium concentrations >10%, the trigonal-rhombohedral phase becomes dominant while residual hexagonal phase persists. This phase evolution confirms that chromium incorporation destabilizes the hexagonal structure through direct iron site substitution, while the trigonal-rhombohedral framework remains more tolerant to chromium inclusion. The structural behavior of $CuCrO_2$, where Cr^{3+} ions occupy octahedral sites creating a geometrically frustrated magnetic lattice, further supports this interpretation. The A-site copper cations maintain their characteristic dumbbell-like linear oxygen coordination throughout these transformations, preserving the fundamental delafossite topology.

To gain atomic-level insight into the structural modifications and electronic perturbations induced by chromium substitution, we conducted comprehensive X-ray absorption fine structure (XAFS) spectroscopy studies. This technique is particularly suited for investigating local coordination environments and electronic configurations due to its exceptional sensitivity to short-range order and element-specific electronic states. The investigation focused on Fe K-edge XAFS measurements performed at room temperature using the SPring-8 synchrotron radiation facility. These spectra originate from dipole-allowed electronic transitions of 1s core electrons to unoccupied p-states above the Fermi level, providing direct information about the oxidation state, local symmetry, and bonding characteristics of iron centers.

Table 1. Structural parameters derived from Rietveld refinement of synchrotron X-ray diffraction patterns for the $CuFe_{1-x}Cr_xO_2$ series (x = 0.00–0.20)

Substitution	Crystal	α	β	γ	a	b	c	Geometry	SG	%
x=0.00	$CuFeO_2$	33.618	33.618	33.618	8.649	8.649	8.649	Trigonal	R-3m:R	87.7
	$CuFeO_2$	90	90	120	6.918	6.918	14.222	Hexagonal	P63/mmc	12.3
x=0.01	$CuFeO_2$	34.234	34.234	34.234	8.454	8.454	8.454	Trigonal	R-3m:R	97.1
	$CuFeO_2$	90	90	120	6.918	6.918	14.222	Hexagonal	P63/mmc	2.0
	$CuCrO_2$	90	90	90	2.810	2.810	11.197	Hexagonal	P63/mmc	0.9
x=0.05	$CuFeO_2$	34.384	34.384	34.384	8.459	8.459	8.459	Trigonal	R-3m:R	88
	$CuFeO_2$	90	90	120	7.039	7.039	13.704	Hexagonal	P63/mmc	7.2
	$CuCrO_2$	90	90	90	2.920	2.920	11.264	Hexagonal	P63/mmc	4.8
x=0.10	$CuFeO_2$	34.269	34.269	34.269	8.466	8.466	8.466	Trigonal	R-3m:R	89
	$CuFeO_2$	90	90	120	7.439	7.439	13.954	Hexagonal	P63/mmc	01.7
	$CuCrO_2$	90	90	90	2.920	2.920	11.264	Hexagonal	P63/mmc	8.3
x=0.15	$CuFeO_2$	34.124	34.124	34.124	8.477	8.477	8.477	Trigonal	R-3m:R	84.2
	$CuFeO_2$	90	90	120	7.392	7.392	13.860	Hexagonal	P63/mmc	0.90
	$CuCrO_2$	90	90	90	2.924	2.924	11.32	Hexagonal	P63/mmc	14.9
x=0.20	$CuFeO_2$	33.600	33.600	33.600	8.542	8.542	8.542	Trigonal	R-3m:R	79.7
	$CuFeO_2$	90	90	120	7.331	7.331	13.722	Hexagonal	P63/mmc	0.70
	$CuCrO_2$	90	90	90	2.974	2.974	11.400	Hexagonal	P63/mmc	19.6

Fig. 3 presents the normalized Fe K-edge absorption spectra for the $CuFe_{1-x}Cr_xO_2$ series (x = 0.01-0.20), revealing systematic variations in the near-edge (XANES) region.

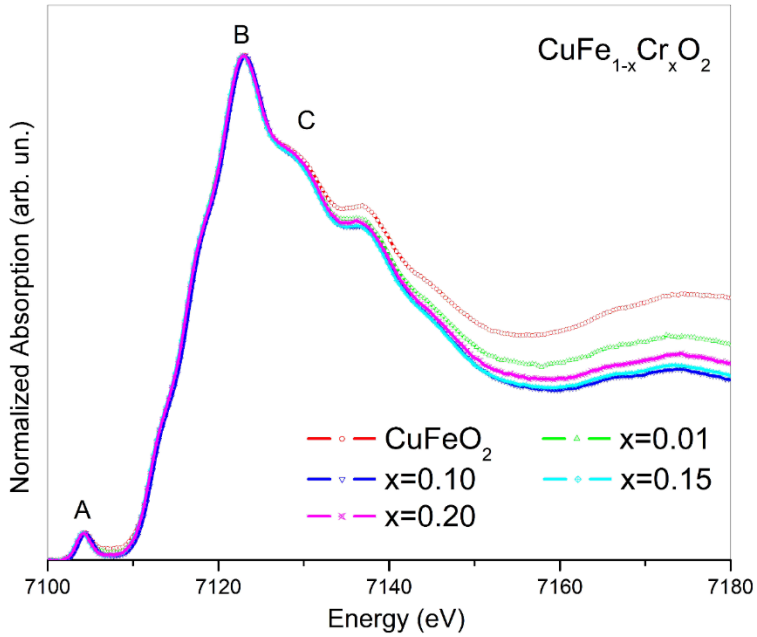

Fig. 3. Normalized X-ray absorption fine structure (XAFS) spectra of the $CuFe_{1-x}Cr_xO_2$ series (x = 0.00-0.20): Fe K-edge XANES region showing the pre-edge (A and B), main edge (C), and post-edge (D) features (colour online)

The XANES region (approximately -20 to +30 eV relative to the edge) reflects the electronic density of states with precise determination of iron oxidation states through edge position analysis, quantification of local structural distortions via EXAFS fitting, evaluation of Cr-induced changes in Fe-O bonding characteristics, and assessment of

next-nearest neighbor interactions in the delafossite framework. Besides, this approach enables direct correlation between chromium incorporation and modifications in the electronic structure and local coordination environment of iron centers, providing crucial insights into the substitution mechanisms and their impact on material properties.

The Fe K-edge X-ray absorption spectra (Fig. 3) reveal several characteristic features that provide insight into the electronic and coordination environment of iron in the $CuFe_{1-x}Cr_xO_2$ system. The absorption onset at 7102 eV marks the Fermi level position, while the weak pre-edge feature A at 7104.17 eV, though formally dipole-forbidden (1s→3d transition), gains intensity through quadrupole transitions and 3d-4p orbital mixing. This feature's persistence across all compositions indicates robust Fe 3d-O 2p hybridization, a signature of strong covalent character in the Fe-O bonds.

The spectral region above the edge shows three distinct features: (1) a shoulder at 7117.88 eV (B) suggesting minor tetrahedral Fe coordination, likely due to oxygen vacancy formation; (2) the dominant peak C at 7122.92 eV corresponding to 1s→4p transitions in octahedrally coordinated Fe^{3+}; and (3) a weak post-edge feature D attributed to metal-metal interactions in the edge-sharing FeO_6 octahedral network. The spectral similarity across all chromium concentrations demonstrates the remarkable stability of the Fe local environment despite Cr substitution. This stability stems from two key factors: first, the substantial electronegativity difference between Fe (1.8) and Cr (1.6) maintains strong Fe-O bonding; second, the pre-edge feature's consistent intensity and position confirm preserved Fe 3d-O 2p hybridization. The system maintains formal oxidation states of Cu^+ and Fe^{3+} throughout the substitution series, with chromium entering as Cr^{3+} to form the $CuCrO_2$ secondary phase, as evidenced by complementary structural data (Fig. 4). This charge conservation explains the observed stability in iron's electronic environment despite the introduction of chromium dopants.

The Cu K-edge X-ray absorption spectra (Fig. 4) reveal distinct electronic and structural characteristics of the copper sites. The absorption threshold at 8962.8 eV corresponds to the 1s ionization energy, while the weakly intense pre-edge feature at approximately 8975 eV arises from formally dipole-forbidden 1s→3d transitions. This feature's diminished intensity in pristine $CuFeO_2$ reflects the highly localized nature of Cu^+ $3d^{10}$ electronic configuration, where minimal 3d-2p hybridization occurs due to filled d-orbitals. The dominant white line peak at 8984.68 eV, corresponding to dipole-allowed 1s→4p transitions, maintains consistent position and intensity across all compositions. This spectral invariance confirms the preservation of monovalent Cu^+ oxidation state ($3d^{10}$ configuration) throughout chromium substitution, consistent with the delafossite structure's requirement for charge balance.

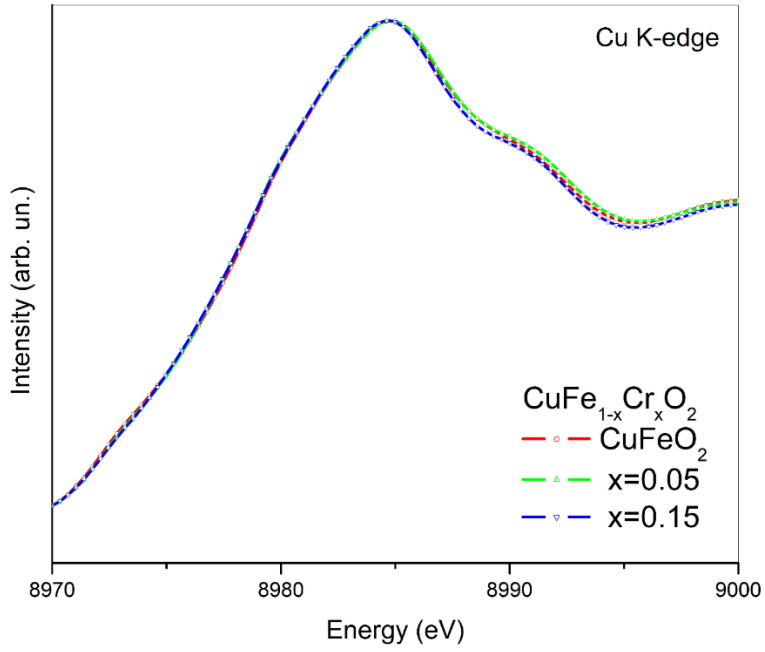

Fig. 4. Cu K-edge normalized XANES spectra for chromium-substituted $CuFe_{1-x}Cr_xO_2$ (x = 0.05, 0.15). All spectra were collected at room temperature in transmission mode (colour online)

In the extended fine structure beyond the XANES region, the photoelectron scattering dynamics provide atomic-scale structural information. As excited photoelectrons propagate outward from the copper absorber, they experience elastic scattering from neighboring atomic potentials that cause phase shifts due to core-level interactions and amplitude reduction from inelastic processes. These quantum mechanical interactions generate the characteristic EXAFS oscillations, which we analyze through Fourier transformation (FT-EXAFS) to

obtain radial distribution functions and curve-fitting to determine bond distances and coordination numbers.

As shown in Fig. 5, the EXAFS scattering data demonstrate high consistency across the sample series, suggesting a stable crystalline environment. EXAFS intensities can be extracted from the XAFS spectra tail according to the following equation:

$$\chi(E) = \frac{\mu(E) - \mu_0(E)}{\mu_0(E)} \quad (1)$$

where μ_0 (E) represents the background absorption and μ(E) is the total absorption. The application of this equation to the XAFS data yields the scattering intensities. A notable shift in the scattering data for the x = 0.10 sample (Fig. 5) indicates alterations in the local atomic environment around the iron atoms.

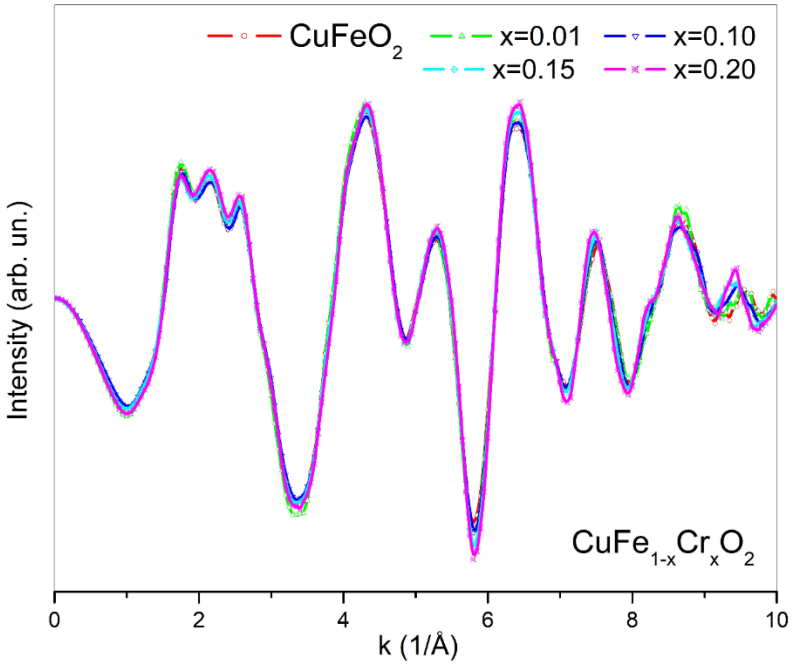

Fig. 5. Fourier-transformed EXAFS scattering data for chromium-substituted $CuFe_{1-x}Cr_xO_2$ (x = 0.00-0.20) (colour online)

Fourier-transformed EXAFS analysis of the $CuFe_{1-x}Cr_xO_2$ series was conducted to probe the local atomic environment surrounding iron centers. The magnitude spectra in Fig. 6 reveal distinct coordination shells, with peak positions corresponding to specific atomic pair correlations. The first coordination sphere, appearing between 1-2 Å, comprises contributions from the Fe-O bonds at 1.816 Å, characteristic of edge-sharing FeO_6 octahedra in both trigonal-rhombohedral and hexagonal phases, and Fe-O interactions at 1.989 Å, reflecting slight distortions in the oxygen coordination environment.

The second coordination sphere (2-4 Å) exhibits Fe-Fe correlations at 3.028 Å, corresponding to metal-metal distances within the octahedral layers and Fe-Cu interactions at 3.343 Å, representing interlayer distances between FeO_6 sheets and Cu^+ cations.

The oxygen anions act as bridging ligands, mediating superexchange interactions between adjacent metal centers. The persistence of these characteristic distances across all compositions indicates that chromium substitution preserves the fundamental structural motifs of both delafossite phases while introducing local disorder, as evidenced by peak broadening in the FT spectra.

The Fourier-transformed EXAFS spectra reveal consistent overall peak profiles across all samples, indicating preservation of the fundamental coordination geometry. However, careful analysis shows a systematic shift of the second coordination shell peak (~3.0 Å) toward lower radial distances with increasing chromium content. This displacement, quantified at 0.05 ± 0.01 Å for x = 0.20, demonstrates measurable contraction in the Fe-(O)-Fe/Cr bond pathways due to Cr^{3+} substitution at iron sites. The observed peak splitting (ΔR = 0.12 Å between components) arises from the local structural relaxation around Cr^{3+} centers, owing to their smaller ionic radius (0.615 Å) compared to Fe^{3+} (0.645 Å), and modified superexchange interactions through Cr-O-Fe pathways. This structural adaptation effectively compensates for potential lattice strain that might otherwise develop from the differing crystallization behaviors of copper and iron sublattices. The maintenance of well-defined EXAFS oscillations despite these changes confirms that the substitution preserves both short-range order and the fundamental delafossite framework.

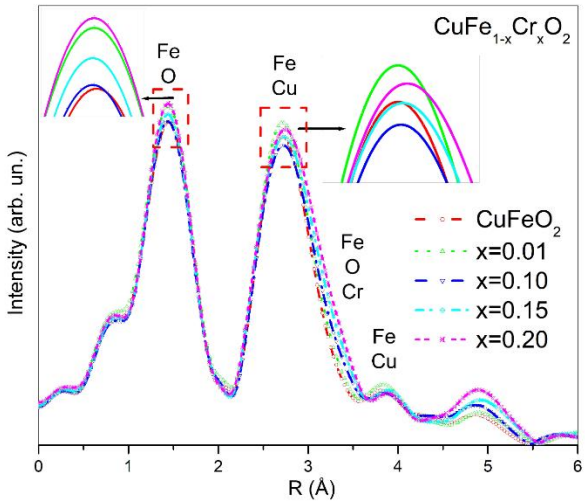

Fig. 6. Fourier-transformed EXAFS (FT-EXAFS) spectra of $CuFe_{1-x}Cr_xO_2$ (x = 0.00-0.20) collected at the Fe K-edge (7112 eV). The inset shows the zoomed data lines makes the shifts more observeable in pristine $CuFeO_2$ (colour online)

The magnetic properties of $CuFe_{1-x}Cr_xO_2$ (x = 0.0, 0.01, 0.02, 0.05, 0.10, 0.20) were investigated through magnetization (M-T) measurements. M-T curves were acquired under zero-field-cooled (ZFC) and field-cooled (FC) conditions in a 500 Oe magnetic field between 10 K and 300 K. For ZFC measurements, samples were cooled to 10 K without a field, followed by field application and warming to 300 K. Conversely, FC measurements involved cooling the samples from room temperature to 10 K in a constant magnetic field. Fig. 7 presents the M-T curves for the $CuFe_{1-x}Cr_xO_2$ series.

Chromium substitution marginally modifies the magnetic behavior of $CuFeO_2$. The bifurcation between ZFC and FC curves diminishes with increasing chromium content. A pronounced bifurcation is observed at low temperatures, characteristic of spin-glass or cluster-glass states. These states lead to frozen random spin orientations, resulting in the divergence of ZFC and FC curves. The suppression of this bifurcation by chromium suggests a reduction in spin-glass-like behavior. Additionally, magnetization at low temperatures increases with chromium doping under a 500 Oe field, possibly due to weakened antiferromagnetic interactions caused by relocalized chromium ions. The transition temperature of all samples exceeded the measurement limit of 300 K.

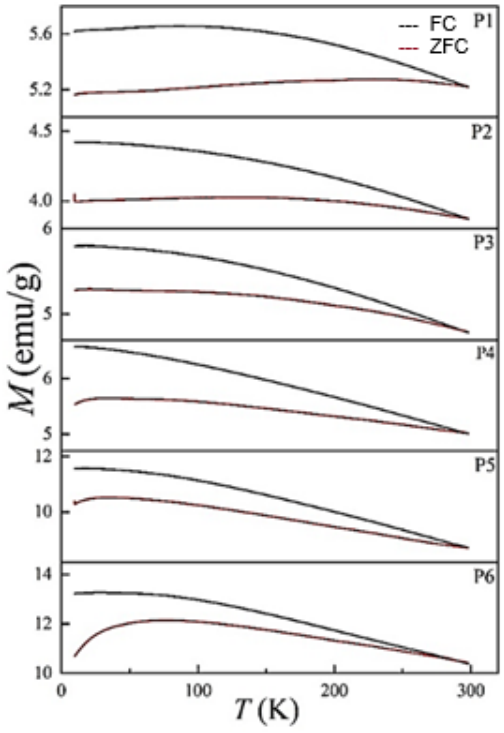

Fig. 7. Temperature dependence of magnetization for $CuFe_{1-x}Cr_xO_2$ samples (x=0.0, 0.01, 0.05, 0.10, 0.15, and 0.20) under Zero-Field-Cooled (ZFC) and Field-Cooled (FC) conditions (colour online)

Fig. 8a-b presents magnetic hysteresis (*M-H*) loops for the samples measured at 10 K and 300 K, respectively. Given the absence of a magnetic phase transition within the studied temperature range, the *M-H* curves exhibit similar soft ferromagnetic behavior at both temperatures. As expected, the saturation magnetization (*Ms*) values are higher at 10 K compared to 300 K due to reduced thermal effects. Fig. 8c illustrates the *Ms* values as a function of chromium content in $CuFe_{1-x}Cr_xO_2$. Ms initially decreases with increasing chromium up to 10% before increasing to a maximum at 20%, potentially related to the emergence of the $CuCrO_2$ phase at higher chromium concentrations. Figs. 8d and 8e show that both coercivity (*Hc*) and remanence (*Mr*) gradually decrease with increasing chromium content. The reduction in *Hc* correlates with the diminished magnetic anisotropy observed in the *M-T* curves.

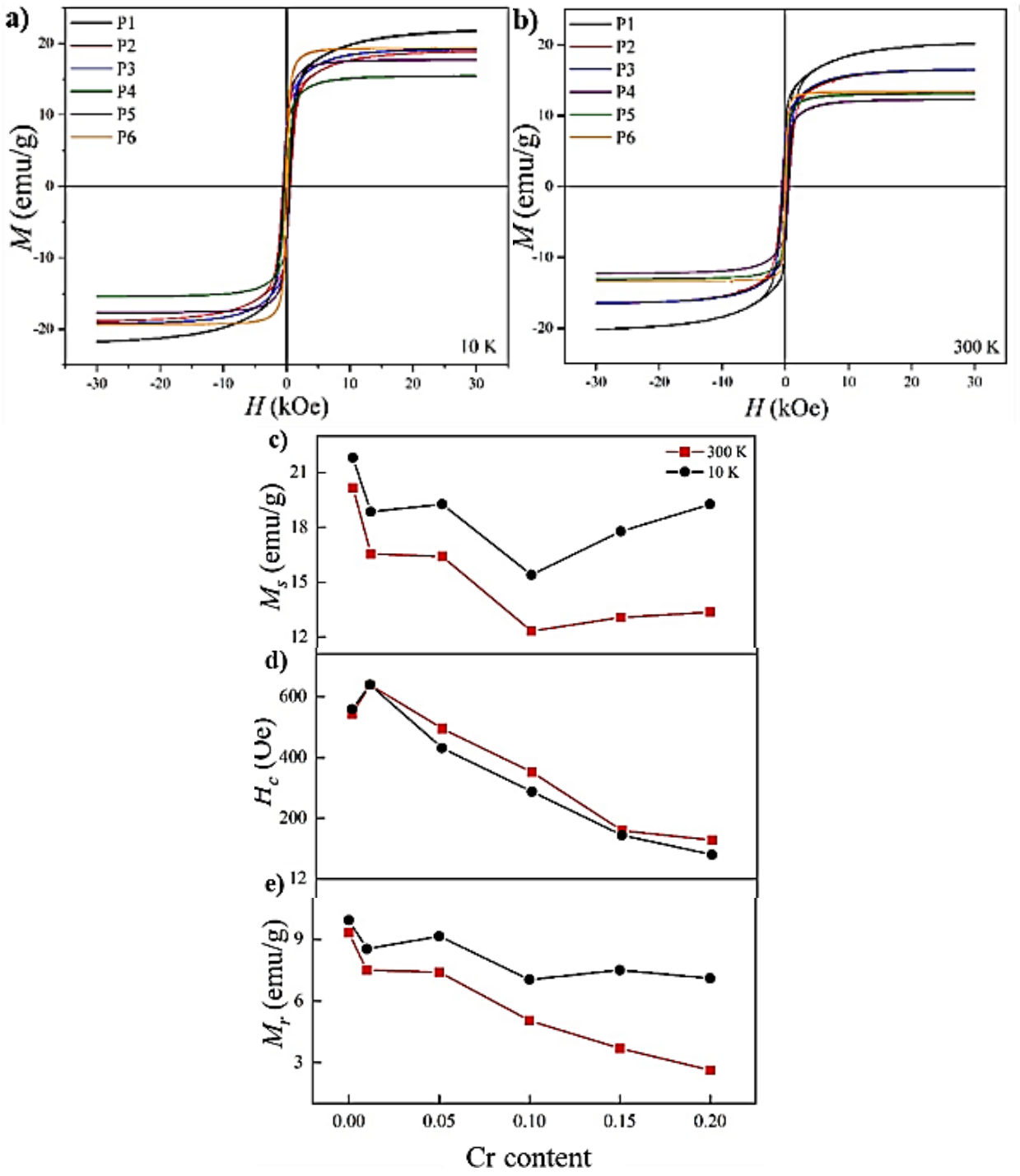

Fig. 8. Magnetic hysteresis loops of $CuFe_{1-x}Cr_xO_2$ samples measured at (a) 10 K and (b) 300 K. Dependence of (c) saturation magnetization, (d) coercive field, and (e) remanence on chromium content in $CuFe_{1-x}Cr_xO_2$ samples (colour online)

4. Conclusions

Our comprehensive investigation employed synchrotron X-ray diffraction (XRD) and X-ray absorption fine structure (XAFS) spectroscopy to probe the room-temperature crystal and electronic properties, complemented by temperature-dependent magnetic measurements (10-300 K) under applied fields. The pristine $CuFeO_2$ displayed a dual-phase composition, with the majority trigonal-rhombohedral phase (R-3m, 87.7 wt%) coexisting with a minority hexagonal polymorph ($P6_3/mmc$, 12.3 wt%) that remained remarkably stable throughout chromium substitution.

Structural analysis revealed that chromium incorporation led to the nucleation of a distinct tetragonal $CuCrO_2$ phase (*$P6_3/mmc$*) while maintaining the host matrix's oxygen stoichiometry. This preservation of anion sublattice integrity stems from the stronger covalent character of Fe-O bonds (Pauling electronegativity difference $\Delta\chi = 1.6$) compared to Cr-O bonds ($\Delta\chi = 1.4$), as confirmed by the unchanged oxygen positional parameters in Rietveld refinement and consistent pre-edge features in O K-edge XAS spectra.

XAFS analysis substantiated the XRD observations by demonstrating retention of Fe^{3+} local coordination geometry despite Cr substitution and minimal disruption to the delafossite framework's medium-range order.

The magnetic properties exhibited unexpected behavior, with all substituted samples showing ferromagnetic characteristics throughout the measured temperature range (10-300 K) with a marked departure from the well-documented antiferromagnetic ordering in pure $CuFeO_2$ below 11-14 K. This modified magnetic behavior suggests chromium-mediated changes in the superexchange interaction network, potentially through the introduction of ferromagnetic Cr^{3+}-O-Cr^{3+} pathways alongside the native antiferromagnetic Fe^{3+}-O-Fe^{3+} couplings.

Acknowledgments

The authors declare that they have no known competing financial interests or personal relationships that could have appeared to influence the work reported in this paper.

XAFS (proposal no. 2022B1663) and SR-XRD (proposal nos. 2022B1664) measurements were performed at the SPring-8 synchrotron facility with approval from the Japan Synchrotron Radiation Research Institute (JASRI).

This study is partly supported by the 2219 program of The Scientific and Technological Research Council of Turkey with Ref. No. 53325897-115.02-152809, and also by Tarsus University BAP Project with Ref. No. MF.23.002.

References

[1] S. Manipatruni, D. E. Nikonov, C. C. Lin, Nature **565**, 35 (2019).
[2] O. M. Ozkendir, Metall. Mater. Trans. A **47**, 2906 (2016).
[3] T. Kongkaew, A. Sinsarp, T. Osotchan, W. Limphirat, K. Subannajui, Materials Today Proceedings **5**(5-1), 10932 (2018).
[4] D. Khomskii, Physics Reports **828**, 1 (2019).
[5] O. Yasuhiro, S. Kenichi, N. Tomohiro, T. Kajitani, Jpn. J. Appl. Phys. **46**, 1071 (2007).
[6] T. Nozaki, K. Hayashi, T. Kajitani, Proceedings ICT'07 - 26th International Conference on Thermoelectrics, 167 (2007).
[7] Z. Deng, X. Fang, S. Wu, W. Dong, J. Shao, S. Wang, M. Lei, Journal of Sol-Gel Science and Technology **71**, 297 (2014).
[8] C. Ruttanapun, P. Jindajitawat, P. Buranasiri, A. Harnwunggmaoung, A. Charoenphakdee, V. Amornkitbamrung, J. Am. Ceram. Soc. **98**, 437 (2015).
[9] F. Matsukura, Y. Tokura, H. Ohno, Nature Nanotech. **10**, 209 (2015).
[10] C. Baratto, R. Kumar, G. Faglia, K. Vojisavljevic, B. Malic, Sensor Actuat. B-Chem. **209**, 287 (2015).
[11] L. Lu, J.-Z. Wang, X.-B. Zhu, X.-W. Gao, H.-K. Liu, J. Power Sources **196**, 7025 (2011).
[12] O. M. Ozkendir, S. Saran, Journal of Electronic Materials **52**(7), 4699 (2023).
[13] S. Kawaguchi, M. Takemoto, H. Tanaka S. Hiraide, K. Sugimoto, Y. Kubota, Y., J. Synchrotron. Rad. **27**, 616 (2020).
[14] T. Uruga, H.Tanida, Y. Yoneda, K. Takeshita, S. Emura, M. Takahashi, M. Harada, Y.Nishihata, Y. Kubozono, T.Tanaka, T. Yamamoto, H. Maeda, O. Kamishima, Y. Takabayashi, Y. Nakata, H. Kimura, S. Goto, T. Ishikawa, J. Synchrotron. Rad. **6**, 143 (1999).
[15] K. Momma, F. Izumi, J. Appl. Cryst. **44**, 1272 (2011).
[16] R. Bencheikh, K. Belakroum, Journal of Nano- and Electronic Physics **14**(5), 05030 (2022).
[17] H. Yang, J. Liang, Q. Cui, Nature Rev. Phys. **5**, 43 (2023).

*Corresponding author : ozkendir@tarsus.edu.tr